

# *A-priori* sparsification of Galerkin based reduced order models

Riccardo Rubini<sup>1†</sup>, Davide Lasagna<sup>1</sup> and Andrea Da Ronch<sup>1</sup>

<sup>1</sup>Faculty of Engineering and Physical Sciences, University of Southampton, SO17 1BJ  
Southampton, UK

(Received xx; revised xx; accepted xx)

In this paper a novel methodology to generate reduced order models with the minimal number of triadic interactions between modal structures is presented. To our goal we define an optimal rotation from a larger to a smaller subspace in modal space, transforming the original POD basis in a new one such that the Galerkin projection onto the rotated bases generates a sparse triadic interaction tensor. This methodology produces, with no *a priori* assumptions on the flow, interpretable, sparsely-connected models that reproduce the original dynamical behaviour at a lower computational cost since less triadic interactions are present in the dynamics. We demonstrate this approach on the lid driven cavity flow at  $Re = 2 \times 10^4$  where the motion is chaotic. We show that the proposed methodology produces a new set of modes generating a reduced order models containing the minimal number of triadic interactions. To understand the role of the dimension of the subspace used to perform the rotation we consider several models with different energy resolution (of dimension  $N$ ) generated from spaces of increasing dimension ( $M$ ). Interestingly, we observe that for each model a minimal value of the density, depending on the ratio  $M/N$ , exists. More importantly, the relevant energy pattern between modal structures are conserved in the sparse system only if the temporal stability is enforced in the procedure confirming that the presence of a dynamically-related constraint is necessary to obtain a physically consistent sparsification.

**Key words:**

---

## 1. Introduction

From a physical standpoint, turbulence is an intrinsically multi-scale phenomenon containing a wide hierarchy of spatial and temporal scales. The intrinsic nonlinearity of the governing equations poses considerable difficulties to its modelling. One of the major limitations is that the dynamics of a single scale cannot be examined in isolation without simultaneously considering the whole hierarchy of complementary scales (Domaradzki *et al.* 1994). In fact, triadic interactions involving scales across the whole hierarchy play a fundamental role, as they are the main driver of energy transfer between coherent structures (Pope 2001; Moffatt 2014). The organisation of such interactions has a direct influence on the physics of a number of flow phenomena, such as direct and inverse energy cascades (Kolmogorov 1991) or transition to turbulence (Craik 1971; Rempfer & Fasel 1994*a,b*) in different flow configurations (Schmidt 2020). These features, in turn, make the

† Email address for correspondence: r.rubini@soton.ac.uk

development of computationally efficient and physically interpretable dynamical models a challenging task.

Historically, the study of triadic interactions has been facilitated by using an appropriate modal decomposition technique to educe coherent structures from the turbulent motion and then using Galerkin projection to characterise the intensity of the inter-modal couplings. For homogeneous isotropic turbulence, Fourier modes provide an optimal representation (Brasseur & Wei 1994; Laval *et al.* 1999). For flow in complex geometries modes identified from data with Proper Orthogonal Decomposition (POD) (Lumley 1970; Couplet *et al.* 2003; Rempfer & Fasel 1994a) or frequency based approaches such as (Symon *et al.* 2020; Schmid 2010; Towne *et al.* 2018) have been typically adopted. [More specifically, frequency based approaches are more suitable for the analysis of statistically stationary flows. In addition, it has been observed that, due to the frequency coupling between modes in Fourier space, these models provide a very compact representation of the triadic interactions.] One of the key findings of such studies is that energy transfers are not equally distributed across scales. Implicit in this picture is the fact that not all interactions have the same importance and the energy flows according to preferential patterns of triads of modes. In fact, extensive numerical evidence suggest that the nonlinear interaction pattern among coherent structures is sparse. In other words, the evolution of structures at a certain length scale depends predominantly upon a subset of all other structures (Kraichnan 1971; Ohkitani 1990; Brasseur & Wei 1994) and the influence of interactions with the complementary set of structures can be generally neglected with minor global effects. This behaviour has been observed for a multiplicity of different flows, ranging from (Symon *et al.* 2020; Jin *et al.* 2020) to (Rempfer & Fasel 1994a,b).

However, these studies have utilised state-of-the-art modal decomposition methods that are inherently targeting optimal data representation. Therefore, these do not model or capture the aforementioned physical features of scale interactions in turbulence, nor include any information regarding the nonlinear structure of the governing equations that produce such interactions. In addition, from a computational standpoint, reduced order models obtained using these techniques do not exploit these features. For example, POD modes have generally global support over the domain (see e.g. Taira *et al.* (2017)). Consequently, the quadratic coefficient tensor appearing in evolution equations is not strictly sparse in the sense employed by Brunton *et al.* (2016). In fact, unless particular symmetries apply, the coefficient tensor is generally dense. This implies that computational costs grows as the third power of the number of modes and the interpretation of scale interactions can be challenging.

To address this challenge, we recently proposed (Rubini *et al.* 2020a) to utilise  $l_1$ -based regression methods (Brunton *et al.* 2016; Loiseau & Brunton 2018) to extract sparsity patterns in an existing, densely connected, Galerkin models, and construct sparse, computationally efficient and interpretable models. The technique involves an *a posteriori* evaluation of energy interactions between a fixed set of modes, pruning weak interactions that do not contribute to the overall dynamics. The downside of this methodology is that the strict link between modal structures and the projection-based model is lost, since the procedure involves a fine tuning of the nonzero model coefficients without modifying the basis functions. Hence, the analysis of the resulting interactions is not necessarily consistent with the spatial structure of the modal functions. In addition, we demonstrated that the structure of energy interactions and its sparsity is not necessarily invariant with respect to a change of the basis functions utilised for the analysis.

To address this gap, we propose in this work a methodology that aims to rigorously

generates a set of modal structures with good energy representation properties such that the resulting interaction coefficient tensor is *a-priori* maximally sparse, without the need of subsequent post-processing or tuning. For this task we utilise POD as a starting point. The key idea is to rotate a set of  $N$  POD modes within a POD subspace of larger dimension  $M$ , to obtain a new set of modes such that the resulting reduced order model has quadratic coefficient tensor with a sparse structure. From an implementation point of view, we find the rotation by solving a constrained optimisation problem, where we seek the rotation that maximises energetic optimality subject to a constraint on the sparsity of the quadratic coefficient tensor.

The manuscript is organised as follows. For completeness, section 2 outlines the general methodology to generate reduced order models by Galerkin projection and how energy interactions between modes defining such models can be carried out. Subsequently, the optimisation problem to generate the new sparse basis function is outlined. In section 3 we demonstrate this methodology by considering Galerkin models of two-dimensional lid driven cavity flow at a Reynolds number  $Re = 2 \times 10^4$ , where dynamics is chaotic (Auteri *et al.* 2002).

## 2. Methodology

### 2.1. Galerkin-based models and energy analysis

We consider the space of square integrable velocity vector fields defined over a spatial domain  $\Omega$ , endowed by the standard inner product defined as,

$$(\mathbf{u}, \mathbf{v}) := \int_{\Omega} \mathbf{u} \cdot \mathbf{v} d\Omega, \quad (2.1)$$

where  $\mathbf{u}, \mathbf{v}$  are two element of such space. The resulting  $\mathcal{L}^2(\Omega)$  norm is denoted as  $\|\mathbf{u}\|_2 = \sqrt{(\mathbf{u}, \mathbf{u})}$ . Using the time averaged velocity field  $\bar{\mathbf{u}}(\mathbf{x})$  as a base flow, and denoting by  $\mathbf{u}'(t, \mathbf{x}) = \mathbf{u}(t, \mathbf{x}) - \bar{\mathbf{u}}(\mathbf{x})$  the velocity fluctuation, a  $N$ -dimensional Galerkin expansion is expressed by the finite sum

$$\mathbf{u}(t, \mathbf{x}) = \bar{\mathbf{u}}(\mathbf{x}) + \mathbf{u}'(t, \mathbf{x}) \sim \bar{\mathbf{u}}(\mathbf{x}) + \sum_{i=1}^N a_i(t) \phi_i(\mathbf{x}). \quad (2.2)$$

This expression is introduced to describe the space-time velocity field, where  $a_i(t)$  and  $\phi_i(\mathbf{x})$ ,  $i = 1, \dots, N$  are the temporal and global spatial modes, respectively. The modes  $\phi_i$  may be computed from numerical or experimental data or *a priori* from a characteristic operator of the system (Taira *et al.* 2017) or from completeness considerations (Noack & Eckelmann 1994). Reduced order models are then derived by projecting the governing equations for incompressible flows onto the subspace defined by the spatial modes (Rowley & Dawson 2017) through the inner product defined in (2.1).

Restricting the analysis to configurations where the boundaries are either no-slip walls or periodic, the pressure term arising from the projection vanishes (Schlegel & Noack 2015). Since the spatial modes define a solenoidal field the system of coupled nonlinear differential equations (ODEs)

$$\dot{a}_i(t) = \mathbf{C}_i + \sum_{j=1}^N \mathbf{L}_{ij} a_j(t) + \sum_{j=1}^N \sum_{k=1}^N \mathbf{Q}_{ijk} a_j(t) a_k(t), \quad i = 1, \dots, N \quad (2.3)$$

is obtained, defining the temporal evolution of the coefficients  $a_i(t)$  and where the tensors  $\mathbf{C}$ ,  $\mathbf{L}$  and  $\mathbf{Q}$  are defined by suitable inner products involving the spatial modes. For

instance, the quadratic coefficients are defined as

$$\mathbf{Q}_{ijk} = (\phi_i, \phi_j \cdot \nabla \phi_k), \quad (2.4)$$

while expressions for the constant and linear terms can be found in Noack *et al.* (2011).

Since the spatial modes satisfy automatically the boundary conditions, the expansion (2.2) provides a suitable foundation to examine interactions between coherent structures in complex geometries. Here, we follow established approaches (Rempfer & Fasel 1994b) and analyse such interactions by introducing the modal energies  $e_i(t) = \frac{1}{2}a_i(t)a_i(t)$ ,  $i = 1 \dots, N$ . For an expansion consisting of  $N$  modes, the domain integral of the kinetic energy of velocity fluctuations is given by NOTA: come chiamiamo questa quantita?

$$E(t) = \frac{1}{2} \sum_{i=1}^N a_i^2(t). \quad (2.5)$$

The instantaneous rate of change of the modal energies is given by

$$\dot{e}_i(t) = C_i a_i(t) + \sum_{j=1}^N L_{ij} a_i(t) a_j(t) + \sum_{j=1}^N \sum_{k=1}^N Q_{ijk} a_i(t) a_j(t) a_k(t), \quad i = 1, \dots, N, \quad (2.6)$$

obtained by multiplying (2.3) by  $a_i(t)$ . The right hand side of equation (2.6) is composed of three terms describing energy transfers between the hierarchy of modes. The first two describe variations of energy due to production/dissipation arising from interactions with the mean flow and from viscous effects (Noack *et al.* 2011). The third term defines variations of energy arising from inviscid nonlinear interactions between triads of modes. Additional insight can be gained by taking the temporal average of equation (2.6), i.e. by examining the time-averaged energy budget of system (2.3). NOTA: occhio alla frase dopo. Since the temporal coefficients have zero mean and are uncorrelated in time, we obtain

$$L_{ii} \overline{a_i a_i} + \sum_{j=1}^N \sum_{k=1}^N Q_{ijk} \overline{a_i a_j a_k} = 0, \quad i = 1, \dots, N, \quad (2.7)$$

showing that, on average, the flow energy balance is regulated by the production/dissipation described in the linear term and by the nonlinear energy transfer described by the quadratic term. As explained in Balajewicz *et al.* (2013), the residual of (2.7) only vanishes when  $N \rightarrow \infty$  and it is generally expected to be positive for finite-dimensional Galerkin models. For conciseness, the tensor  $\mathbf{N}$  with entries

$$N_{ijk} = Q_{ijk} \overline{a_i a_j a_k}, \quad (2.8)$$

is introduced. The study of the properties of this term represents one of the main focus when it comes to perform physically consistent sparsification of the model. NOTA: aggiustare frase sopra.

## 2.2. Subspace Rotation Technique

We now describe the technique employed to rotate the original POD modes into a new set of orthonormal basis functions that produce a sparser Galerkin model and outline the optimisation procedure used to find the optimal rotation.

Let  $\mathbf{D}(\mathbf{x}_i, t_k) \in \mathbb{R}^{N_s \times N_t}$  be a matrix collecting the set of time snapshots of the fluctuating velocity field  $\mathbf{u}'(t, \mathbf{x})$ . In the time domain the data is sampled with a temporal discretisation  $t_k = (k-1)\Delta t$   $k = 1, \dots, N_T$ . In the space domain the data is sampled on a grid composed by  $N_s$  grid-points. After reshaping each snapshot in a

column vector  $d_k^i$  the snapshots matrix reads

$$\mathbf{D} = \begin{pmatrix} d_1^1 & \dots & d_{N_T}^1 \\ \vdots & \ddots & \vdots \\ d_1^{N_s} & \dots & d_{N_T}^{N_s} \end{pmatrix}. \quad (2.9)$$

The matrix  $\mathbf{D}$  can be approximated as matrix multiplication between the matrices  $\mathbf{A} \in \mathbb{R}^{N_t \times M}$  containing in the columns the temporal mode  $a_i(t)$  defined as

$$\mathbf{A} = \begin{pmatrix} a_1(t_1) & \dots & a_M(t_1) \\ \vdots & \ddots & \vdots \\ a_1(t_{N_T}) & \dots & a_M(t_{N_T}) \end{pmatrix} \quad (2.10)$$

and the one containing the spatial modes  $\mathbf{U} \in \mathbb{R}^{N_s \times M}$  as

$$\mathbf{U} = \begin{pmatrix} \phi_1(x_1) & \dots & \phi_M(x_1) \\ \vdots & \ddots & \vdots \\ \phi_1(x_{N_s}) & \dots & \phi_M(x_{N_s}) \end{pmatrix} \quad (2.11)$$

Thus we can approximate the snapshots matrix  $\mathbf{D}$  as multiplication of the two matrices previously defined.

$$\mathbf{D} \sim \mathbf{U}\mathbf{A}^\top, \quad (2.12)$$

where the superscript  $\top$  is the matrix transposition operator. This expression is the matrix equivalent to (2.2) with  $M = N$ , if  $M = N_T$  the equality in (2.12) holds. In this work we follow the idea proposed in Balajewicz *et al.* (2013, 2016), seeking for linear transformation from a larger to a smaller POD subspace defined by the matrix  $\mathbf{X} \in \mathbb{R}^{M \times N}$  satisfying  $\mathbf{X}^\top \mathbf{X} = \mathbf{I} \in \mathbb{R}^{N \times N}$ , necessary to ensure that the rotated basis remains orthogonal. We aim to find a new set of modes, as a linear combination of the original modes, defined by the column of  $\mathbf{X}$ , such that the new model (2.3) generated by Galerkin projection onto the new modal basis has a quadratic interaction tensor  $\mathbf{Q}$ , defined by the scalar product (2.4), with a sparse structure.

The new basis, indicated with a tilde is linked to the original POD basis by the linear transformation:

$$\tilde{\mathbf{U}} = \mathbf{U}\mathbf{X} \quad \text{and} \quad \tilde{\mathbf{A}} = \mathbf{A}\mathbf{X}. \quad (2.13)$$

Subsequently, we define a diagonal matrix containing the eigenvalues of the decomposition in terms of (2.10) as  $\mathbf{\Lambda} = \mathbf{A}^\top \mathbf{A} = \lambda_i \delta_{ij}$ , with  $\lambda_i = \overline{a_i a_i}$ . Its trace, denoted as  $Tr(\mathbf{\Lambda})$ , defines the amount of kinetic energy reconstructed by the modal decomposition. Consequently, the modal energies of the rotated basis is then

$$\tilde{\mathbf{\Lambda}} = \tilde{\mathbf{A}}^\top \tilde{\mathbf{A}} = \mathbf{X}^\top \mathbf{A}^\top \mathbf{A} \mathbf{X} = \mathbf{X}^\top \mathbf{\Lambda} \mathbf{X}. \quad (2.14)$$

If  $\mathbf{X}$  is a square matrix (*i.e.*  $M = N$ ) then  $\tilde{\mathbf{D}} = \mathbf{D}$  follows from (2.12). The energy reconstructed by new basis is the same as that of the original POD basis since  $Tr(\tilde{\mathbf{\Lambda}}) = Tr(\mathbf{\Lambda})$  and because the trace of a matrix is invariant under rotations. It will be shown later that this configuration always leads to unfeasible solutions and is not a suitable choice. Conversely, the values of  $M$  and  $N$ , defining the size of the starting space and of the arrival space, are free parameters and their values affect the properties of the new modal basis.

The coefficients of the Galerkin system (2.3) projected in the new subspace are then

$$\tilde{\mathbf{Q}}_{ijk} = \mathbf{Q}_{pqr} \mathbf{X}_{pi} \mathbf{X}_{qj} \mathbf{X}_{rk} \quad (2.15)$$

$$\tilde{\mathbf{L}} = \mathbf{X}^\top \mathbf{L} \mathbf{X} \quad (2.16)$$

$$\tilde{\mathbf{C}} = \mathbf{X}^\top \mathbf{C}. \quad (2.17)$$

where  $i, j, k = 1, \dots, N$  and  $p, q, r = 1, \dots, M$  and the repeated indices,  $p, q, r$ , are saturated according to the Einstein notation.

The goal is to seek a rotation where the quadratic interaction tensor  $\tilde{\mathbf{Q}}$  has a sparse structure. Mathematically, this rotation can be found as the solution of an optimisation problem composed by two building blocks. The first term aims to minimise the error between the snapshots matrix  $\mathbf{D}$  and the one resulting from the rotation  $\tilde{\mathbf{D}}$ . Once we define the error matrix  $\mathbf{E}$  as  $\mathbf{E} = \mathbf{D} - \tilde{\mathbf{D}}$  we want to minimise the quantity

$$\frac{1}{N_T} \text{Tr}(\mathbf{E}^\top \mathbf{E}) \quad (2.18)$$

where the inner product between error fields can potentially be modified by an suitable weight matrix  $\mathbf{W}$  depending on the discretization scheme. Recalling the definition of  $\mathbf{A}$  the expression 2.18 is equivalent (as shown in appendix ?? ) to

$$\text{Tr}(\mathbf{A} - \mathbf{X}^\top \mathbf{A} \mathbf{X}) = \text{Tr}(\mathbf{A} - \tilde{\mathbf{A}}). \quad (2.19)$$

The second term promotes sparsity in the rotated tensor  $\tilde{\mathbf{Q}}$  and is introduced as a constraint on the  $l_1$  norm of  $\tilde{\mathbf{Q}}$ , following the  $l_1$ -based optimisation approach already used in the sparsification and stabilisation of reduced order models in (Rubini *et al.* 2020a).

The problem is then formulated as follows:

$$\underset{\mathbf{X}}{\text{minimize}} \quad \text{Tr}(\mathbf{A} - \mathbf{X}^\top \mathbf{A} \mathbf{X}) \quad (2.20a)$$

$$\text{subject to} \quad \|\tilde{\mathbf{Q}}\|_1 \leq \xi^{-1} \|\mathbf{Q}\|_1, \quad (2.20b)$$

$$\mathbf{X}^\top \mathbf{X} = \mathbf{I}. \quad (2.20c)$$

with  $\xi$  a free parameter. The underlying idea is that increasing the penalisation weight  $\xi$  decreases the value of  $\|\tilde{\mathbf{Q}}\|_1$  as some of the entries of  $\tilde{\mathbf{Q}}$  are shrunk to zero by the non-differentiability of the  $l_1$  norm Tibshirani (2013); Friedman *et al.* (2008). This optimisation problem is non-convex because of the constraint 2.20c(c), involving polynomials in the optimisation variables, the entries of the matrix  $\mathbf{X}$ , up to order three. The important consequence is that the solution might not be unique and many local minima, corresponding to different sets of basis functions can be obtained. The effects of different initial conditions on the solution is discussed later on in the paper as well as in a more detailed manner in appendix B.

In the first phase of this work we solved problem (2.20c), called *P1* for practical convenience, for increasing values of  $\xi$  obtaining different ROMs with different sparsity. However, we observed that all the modes were neither sparsified in a physically consistent way nor temporally stable, some of these results will be shown later. This showed the need of additional conditions to sparsify the model in a physically consistent manner.

It is a well known issue of Galerkin based reduced order models the presence of an overshoot of kinetic energy due to the loss of information about the small scales implicit in the truncation process. The lost physics needs to be taken into account in the optimisation problem. Classically, this issue is tackled introducing a LES-like sub-grid dissipation model (Noack *et al.* 2005; Östth *et al.* 2014; Galletti *et al.* 2004). In this work, it is

convenient due to the mathematical formulation used to follow the approach proposed in (Balajewicz *et al.* 2013, 2016), where the eigenvalues of the linear part of the Galerkin system  $\mathbf{L}$  are used as proxy of viscous dissipation. In practice, we augment problem (2.20c) with the additional constraint

$$\text{Tr}(\mathbf{X}^\top \mathbf{L} \mathbf{X}) = -\eta \quad (2.21)$$

where  $\eta \in \mathbb{R}^+$  is such that the quantity

$$\chi(\eta) = \frac{\overline{E(t)} - \overline{E_{DNS}(t)}}{\overline{E_{DNS}(t)}}, \quad (2.22)$$

namely the relative difference of the long-time average fluctuation kinetic energy between DNS and numerical simulation of the new model, reaches zero. In practice, the constant  $\eta$  controls the internal dissipation of the model by modifying the eigenvalues of  $\tilde{\mathbf{L}}$ . As observed by Balajewicz *et al.* (2013), this constant is not known *a priori*, but can be found by an extra optimisation loop to ensure that the excess of turbulent kinetic energy is zero.

Taking into account this additional constraint, problem (2.20c) becomes

$$\underset{\mathbf{X}}{\text{minimize}} \quad \text{Tr}(\mathbf{A} - \mathbf{X}^\top \mathbf{A} \mathbf{X}) \quad (2.23a)$$

$$\text{subject to} \quad \text{Tr}(\mathbf{X}^\top \mathbf{L} \mathbf{X}) = -\eta, \quad \text{s.t.} \quad \chi(\eta) = 0, \quad (2.23b)$$

$$\|\tilde{\mathbf{Q}}\|_1 \leq \xi^{-1} \|\mathbf{Q}\|_1, \quad (2.23c)$$

$$\mathbf{X}^\top \mathbf{X} = \mathbf{I}. \quad (2.23d)$$

In this formulation, denoted as P2 henceforth, there is still only one free parameter,  $\xi$ , since  $\eta$  is a dummy variable used to enforce (2.22). It will be shown later on that constraint (2.23d)-(b) is of paramount importance to obtain a physically sound reduced order model.

Problem (2.23d) was solved with the open-source package for nonlinear and non-convex optimisation NLOpt (Johnson 2014). We utilised a gradient-based solver implementing the Method of Moving Asymptotes (MMA) algorithm (Svanberg 2014). The key element to make the procedure viable is to evaluate the sparsity-promoting constraint and its gradient as efficiently as possible. An efficient methodology leading to costs scaling as  $\mathcal{O}(MN^3)$  can be derived and is discussed in appendix C. More importantly, computational costs are not symmetric in  $M$  and  $N$  since generating systems from large starting space dimension  $M$  does not significantly affect the overall computational cost, which are instead dominated by the cubic term  $N^3$ . This is a key aspect since, as it will be shown later, lower densities can be obtained with higher ratios  $M/N$ .

Once (2.23d) is solved, a new set of temporal and spatial modes can be found according to (2.13) while a new set of coefficients for the reduced order model can be found from (2.15). Since the value of  $\xi$  is arbitrary, it can be varied to obtain models with different sparsity. To formalise this concept we introduce the model density, defined as

$$\rho = \frac{\|\tilde{\mathbf{Q}}\|_0}{\|\mathbf{Q}\|_0} \quad (2.24)$$

where  $\|\mathbf{Q}\|_0$  counts the nonzero elements of the tensor  $\mathbf{Q}$ . This can also be expressed as the average of the modal densities  $\rho_i$  as:

$$\rho = \frac{1}{N} \sum_{i=1}^N \rho_i \quad \text{with} \quad \rho_i = \frac{\|\tilde{\mathbf{Q}}_i\|_0}{\|\mathbf{Q}_i\|_0}. \quad (2.25)$$

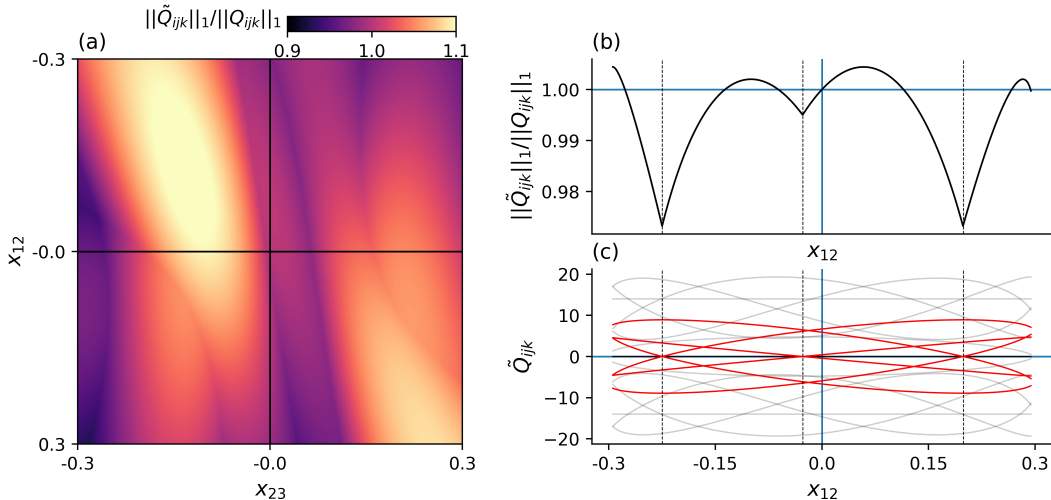


FIGURE 1. Map of  $\|\tilde{\mathbf{Q}}\|_1/\|\mathbf{Q}\|_1$  projected on the  $X_{12} - X_{23}$ , panel (a). One dimensional cut of the same quantity by varying the coordinate  $X_{12}$ , panel (b). The twenty-seven entries  $\tilde{Q}_{ijk}$  as a function of  $X_{12}$ . The six entries that vanish identically in correspondence of the spikes of  $\|\tilde{\mathbf{Q}}\|_1$  are highlighted in red.

To express the loss of energy captured by the rotated basis, we also introduce the global energy reconstruction factor

$$e_N = \frac{\sum_{i=1}^N \tilde{\lambda}_i}{\sum_{i=1}^{N_T} \lambda_i} \quad (2.26)$$

where  $\tilde{\lambda}$  and  $\lambda$  the modal energies of the rotated and original basis, respectively. By definition, the global energy reconstruction factor is always lower than 1.

The density and reconstruction factor are affected by the dimensions  $M$  and  $N$  and by the penalisation weight  $\xi$ . To characterise the effects of these parameters, we can visualise in what follows the generated systems onto the  $\rho - e_N$  plane, similar to the approach used in Rubini *et al.* (2020a).

### 2.3. Sparsity-promoting effect of the $l_1$ -based constraint

To understand heuristically the role of constraint (cr), we consider here a small reduced order model of the lid-driven cavity flow considered later in section 3. A more formal discussion based on the proximity operator theory could also be formulated, using the classical LASSO formulation as a starting point (Friedman *et al.* 2008). To easily visualise the effect of the rotation on the properties of the coefficient tensor  $\tilde{\mathbf{Q}}$ , we consider a small model with dimensions  $M = 5$  and  $N = 3$  and perform a parametric study on the effects of some of the entries of  $\mathbf{X}$  on the quantity  $\|\tilde{\mathbf{Q}}\|_1$  without solving (2.20c), but simply applying the definition (2.15). Figure 2.3-(a) shows contours of  $\|\tilde{\mathbf{Q}}\|_1/\|\mathbf{Q}\|_1$  on the  $X_{12} - X_{23}$  plane, with all other off-diagonal entries of  $\mathbf{X}$  set to zero. Several sharp-bottomed valleys and local minima can be observed, arising from the non-convex, non-smooth nature of the quantity  $\|\tilde{\mathbf{Q}}\|_1$ . Panel (b) shows a cut of panel (a) along the  $x_{12}$  coordinate. Here too, we observe such structure where the minima are identified in the plot by the dashed vertical lines. More interestingly, each minimum corresponds to a point with discontinuous first derivative, due to the nature of the  $l_1$  norm and some entries  $\tilde{Q}_{ijk}$  crossing the zero axis. This behaviour is illustrated in panel (c) where the



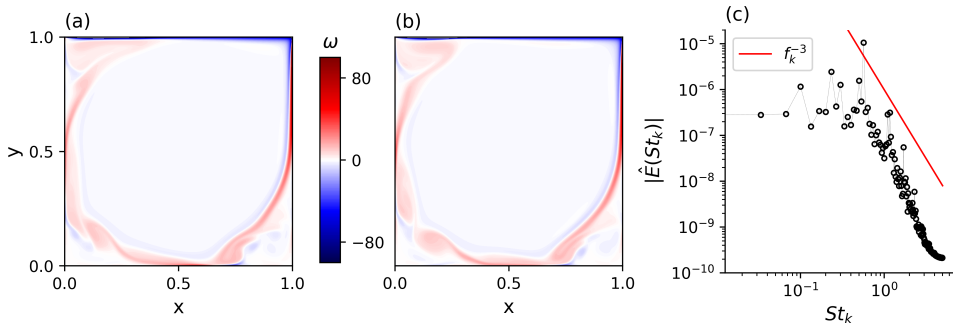


FIGURE 2. Vorticity field  $\omega$  for two different flow snapshots in panels (a) and (b). Amplitude of the Fourier transform of the fluctuating kinetic energy signal (equation 2.5), in panel (c). [metti i ticks in (b), stacca la colorbar, magari colormap, St alla meno tre, metti  $\hat{E}(St)$ , check  $1/\delta t$ ]

entries  $\tilde{\mathbf{Q}}$  are shown, with those crossing the zero for some value of  $X_{12}$  highlighted in red. The general idea is that increasing the penalisation weight  $\xi$  in the sparsity promoting constraint (2.20c)-(c) pushes  $\|\mathbf{Q}\|_1$  closer and closer to one this valleys. In practice, some entries  $\tilde{Q}_{ijk}$  are forced to zero due to the strong gradient at the point of non-differentiability, resulting in a sparse coefficient tensor  $\tilde{\mathbf{Q}}$ . However, unlike in the a-posteriori LASSO-based sparsification methods Brunton *et al.* (2016); Rubini *et al.* (2020a), not all quadratic coefficients can be simultaneously set to zero by an arbitrary rotation, as clear from panel (c). In fact, the tensor  $\tilde{\mathbf{Q}}$  depends nonlinearly on the rotation  $\mathbf{X}$ , while in LASSO-based methods the tensor coefficients are directly the optimisation variables of the problem.

### 3. Demonstration: 2D lid-driven unsteady cavity flow

We now apply this methodology to two-dimensional unsteady flow in a lid-driven square cavity. This is an established test case for the development and validation of model order reduction techniques (Cazemier *et al.* 1998; Terragni *et al.* 2011; Balajewicz *et al.* 2013; Arbabi & Mezić 2017; Fick *et al.* 2018), and we thus consider it here as an exemplar to demonstrate the ideas discussed in the introduction. This is the same test case we utilised in our previous work (Rubini *et al.* 2020a) to demonstrate the properties of the  $l_1$ -based sparsification technique on Galerkin models of multi-scale chaotic flows.

#### 3.1. Problem definition and Proper Orthogonal Decomposition analysis

The Reynolds number is defined as  $Re = LU/\nu$  where  $L, U$  are the cavity dimension and the lid velocity, respectively, and  $\nu$  is the kinematic viscosity. All physical variables introduced later on are scaled with  $L, U$  and combinations thereof. In this work, we consider the flow regimes establishing at  $Re = 2 \times 10^4$ , where the motion is chaotic (Auteri *et al.* 2002; Peng *et al.* 2003). The domain is defined by the nondimensional Cartesian coordinates  $\mathbf{x} = (x, y)$ , and the velocity vector  $\mathbf{u}(t, \mathbf{x})$  is defined by the components  $u(t, \mathbf{x})$  and  $v(t, \mathbf{x})$ . For visualisation purposes, we introduce the out-of-plane vorticity component  $\omega = \partial v / \partial x - \partial u / \partial y$ . Numerical simulations were performed in **OpenFOAM** with the unsteady incompressible flow solver **icofoam**. The convective and viscous terms are spatially discretised with a second-order finite-volume technique and the temporal term with a semi-implicit Crank-Nicholson scheme. A grid independence study was performed, examining average and unsteady flow quantities on increasingly finer meshes. The final

---

$n$	1	5	10	20	30	40	60	80	90	120
$e_N$	0.26	0.74	0.9	0.96	0.97	0.98	0.985	0.99	0.995	0.998

---

TABLE 1. Normalised cumulative energy distribution  $e_N$  for POD modes.

mesh is composed of  $300 \times 300$  cells, with refinement at the four cavity boundaries. This mesh is sufficiently fine to resolve the unsteady high shear regions bounding the main vortex, the high vorticity filaments characteristic of two-dimensional turbulence as well as the spatial structure of the lowest energy POD modes utilised in this study. Similar grid resolutions have been used by Cazemier *et al.* (1998) at similar Reynolds numbers.

Two snapshots of the vorticity field obtained from these simulations are shown in figure 3.1-(a,b). Most of the dynamically interesting features in this regime originate at the bottom-right corner of the cavity. Specifically, the secondary vortex in the recirculation zone is shed erratically, producing wave-like disturbances advected along the shear layer bounding the primary vortex. These structures produce a strong quasi-periodic oscillation of the turbulent kinetic energy, as shown in panel (c), where the amplitude of the Fourier transform of the fluctuation kinetic energy signal (equation 2.5) is shown. Due to the chaotic nature of the flow, the energy spectrum has a strong broadband component with energy uniformly distributed across all the frequencies/spatial structures of the flow. This implies that unlike for periodic flows (Noack *et al.* 2011; Symon *et al.* 2020), the mean triadic interaction tensor  $\mathbf{N}$  is dense with energy transfers highly scattered in modal space. However, the wave-like motion characterising the shear layer dynamics produces a strong energy peak at a characteristic non-dimensional Strouhal number  $St = 0.7$ .

From these simulations, after initial transients have decayed, we extract  $N_T = 1500$  velocity snapshots using a nondimensional sampling period  $\Delta t = 0.1$ . These settings are sufficient to adequately time-resolve the fastest scales of motion as well as to include many shedding events originating at the bottom right corner. The snapshot Proper Orthogonal Decomposition of this dataset is then performed. Table 1 shows the normalised cumulative reconstructed energy (equation (2.26)) by the models utilised in what follows.

### 3.2. Energy analysis and temporal integration of the dense system

We first analyse the properties of the tensors  $\mathbf{Q}$  and  $\mathbf{N}$ , using a reference dense Galerkin model constructed from projection of  $N = 30$  POD modes. Figure 3.2-(a) shows the organisation of the coefficients  $Q_{ijk}$ , using the slice at  $i = 1$  as an illustrative example. The tensor is dense as most coefficients are nonzero. No clear structure in the distribution of the coefficients can be observed except for a slight asymmetry where coefficients for  $k > j$  are typically larger in magnitude, valid for all indices  $i$ . The asymmetry is a consequence of the definition of the quadratic coefficient tensor (2.4), characterising the convective transport, and the range of spatial length scales described by the POD modes, as already observed in Rubini *et al.* (2020a).

The average triadic interactions can be similarly analysed. Figure 3.2-(b) shows the slice of the tensor  $\mathbf{N}$  at  $i = 1$ , where the base ten logarithm of the absolute value of its entries is reported. All entries of  $\mathbf{N}$  are generally nonzero, although the strength of the interactions varies across several orders of magnitude. This is the combined result of the structure of the projection coefficients tensor  $\mathbf{Q}$  and of the complex spectral structure of the temporal coefficients  $a_i(t)$ . Consequently, the interactions are highly organised and there exists a subset of interactions that are more active. To characterise energy paths,

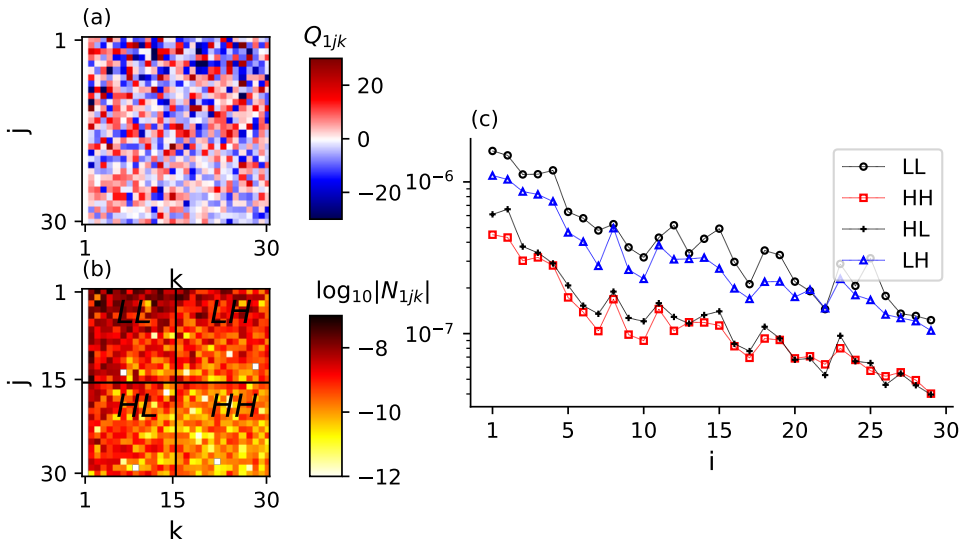


FIGURE 3. Value of the entries of  $\mathbf{Q}$  and absolute value in base ten logarithmic scale of  $\mathbf{N}$  for  $i = 1$  in panel (a) and (b), respectively. Panel (c): sum of the entries of  $\mathbf{N}$  in the four regions defined in panel (b) as a function of the modal index  $i$ .

we split interactions in four regions, denoted as  $LL$ ,  $LH$ ,  $HL$  and  $HH$ . With  $L$  and  $H$  denoting low and high index modes, respectively, these four regions represent a coarse-grained grouping of interactions between scales resolved by the  $N = 30$  decomposition, assuming that low index modes map to the largest scales of motion in the cavity and high modes describe small-scale, low-energy features. Here, we arbitrarily select the split at half of the spectrum ( $N = 15$ ), but other choices are possible and do not change the following results qualitatively. We then compute the sum of the absolute value of the entries  $N_{ijk}$  contained in these four regions. The result is shown in figure 3.2-(d), against the modal index  $i$ . First, energy transfers in the regions  $LL$ ,  $HL$  and  $LH$  are generally more intense than those in region  $HH$ . This follows from the observation that large-scale/large-scale and large-scale/small-scale interactions are more relevant with respect the small-scale/small-scale interactions, across the entire hierarchy. In addition, we observe that the interactions  $LH$  are always larger than the  $HL$  interactions. This is consequence of the asymmetry previously observed in the tensor  $\mathbf{Q}$  and not of the temporal coefficients. This asymmetry is in agreement with the picture of energy transfers between scales in homogeneous isotropic two-dimensional turbulence (Ohkitani 1990; Laval *et al.* 1999), where the large scales interact with the small ones in a non-local fashion.

### 3.3. Model sparsification

Because of the sparsity-promoting constraint, the optimisation problem (2.23d) is non-convex, i.e. there exist potentially many different optima. In the first phases of the research, we have conducted optimisation tests to understand and quantify the role that the initial guess has on the quality of the optimal solution. Our tests show that, starting from small perturbations of the original POD basis leads consistently to the same optimal solution. The results shown henceforth have thus been obtained with this approach. This agrees with our original motivation, *i.e.* to obtain a basis as close as possible to the energy optimal POD that leads to a sparser energy interaction pattern. These tests are omitted here for reasons of brevity, but are reported in appendix B.

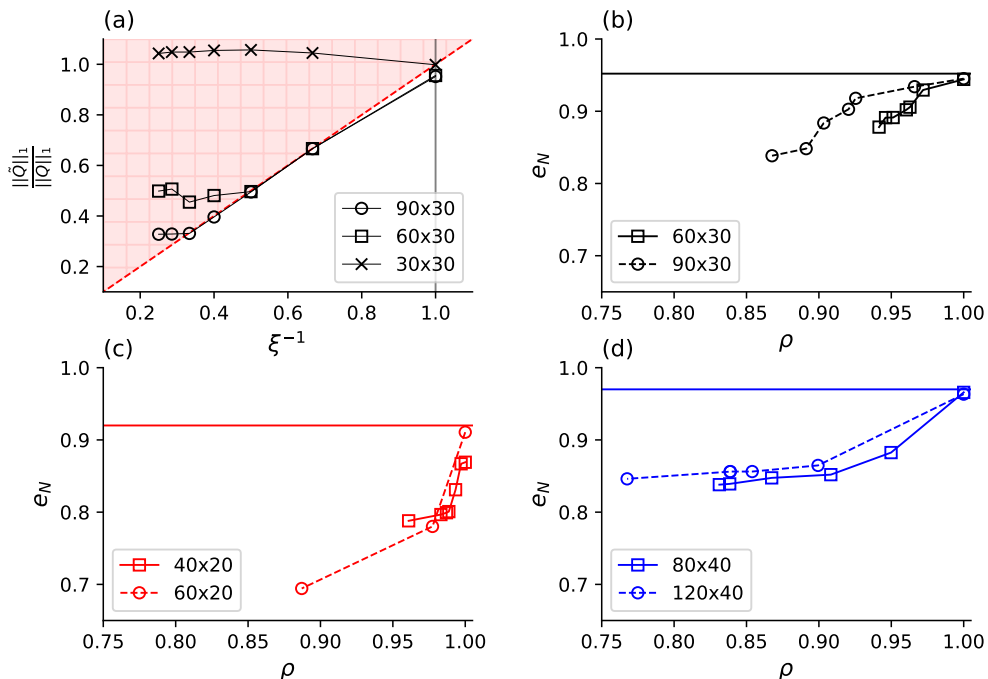


FIGURE 4. Panel (a): visualisation of the sparsity-promoting constraint (2.23d) on the plane  $\xi^{-1}-\|\tilde{\mathbf{Q}}\|_1/\|\mathbf{Q}\|_1$ . The red region denotes the infeasible set. Panels (b) to (d):  $\rho - e_N$  curves for families of models with dimension  $N = 30, 20, 40$  and ratios  $M/N = 2, 3$  (open squares and open circles, respectively).

We consider families of models with  $N = 20, 30$  and  $40$  (see table 1 for the energy resolution), generated from rotations of the original POD basis modes in subspaces of increasing dimension  $M$ . As discussed in section 2, when the starting subspace dimension  $M$  is equal to  $N$ , the stability constraint (2.23d)-(b) can never be satisfied, *i.e.* no solution is acceptable or useful. This behaviour was observed by Balajewicz *et al.* (2016), who pointed out that the case  $M = N$  must be discarded since no temporal stabilisation can be achieved. Hence, we show here results for ratios  $M/N = 2, 3$ . Because of the definition of problem (2.23d), a family of models with different densities  $\rho$  and reconstructed kinetic energy can be generated by varying the penalisation parameter  $\xi$ . In practice, this is achieved by progressively increasing  $\xi$  starting from 1, where the sparsity-promoting constraint is not active, and obtaining  $\eta$  iteratively to ensure long-term temporal accuracy.

We first consider models generated with  $N = 30$  basis modes for increasing ratios  $M/N$ . Figure 3.3-(a) displays optimal solutions on the plane  $\xi^{-1}-\|\tilde{\mathbf{Q}}\|_1/\|\mathbf{Q}\|_1$ . The red dashed line separates solutions that satisfy the sparsity-promoting constraint (2.23d)-(c) (white area) from solutions that do not (red area). Note that all solutions satisfy the stability constraint, so the white region will be referred to as the feasibility region. For the sake of completeness, we report in 3.3-(a) solutions for  $M/N = 1$ . In addition to not satisfying the stability constraint, it can be observed that no solution in the feasible region can be found. Considering now data points for  $M/N = 2$ , for small  $\xi$ , the optimisation problem has feasible solutions generally falling on the boundary of the feasibility region. However, there exists a thresholds value of  $\xi$  above which the optimisation problem terminates unsuccessfully in the unfeasible region. This is manifested in panel (d) by a

sudden turn of the solution traces from the feasible region boundary upwards into the red region. Crucially, this threshold value increases for larger ratios  $M/N$ , *i.e.*, a more pronounced sparsification can be achieved for larger dimensions of the starting subspace. This is arguably a consequence of the fact that higher ratios  $M/N$  corresponds to more degrees of freedom available in 2.23d to ensure that the sparsity constraint is satisfied. From a mathematical point of view, this behaviour is a direct consequence of the fact that a simple rotation of the basis modes, defined by the matrix  $\mathbf{X}$ , cannot shrink to zero an arbitrarily large number of coefficients in the tensor  $\mathbf{Q}$ . At a first glance, the fact that a limiting value of the sparsification can be achieved for any given system may appear as a limitation of the present *a-priori* method. However, this is actually an advantage with respect to the *a-posteriori* LASSO-based model sparsification technique (Rubini *et al.* 2020a). In that case, feasible solutions could always be found for arbitrarily large regularisation weights, where all system coefficients are shrunk to zero in the limiting case. These models, however, were observed to have little physical significance. For instance, in the limiting case with zero density the models would not capture any temporal fluctuation, *i.e.* resulting in the trivial system  $\dot{a}_i(t) = 0, i = 1, \dots, N$ . With the present *a-priori* sparsification method, all feasible systems are temporally stable and provide physically consistent predictions. Therefore, there is no ambiguity linked to the choice of  $\xi$  for a given  $M/N$ , since the feasible model obtained at the largest  $\xi$  (smaller density) should be selected. In what follows we will adopt this approach.

When the penalisation  $\xi$  is increased, sparser models are obtained from the optimisation through small rotations of the original POD basis. This, however, comes at the cost of decreasing the energy optimality of the resulting basis. This effect can be visualised on the  $\rho - e_N$  plane, as shown in figures 3.3-(c, b,d), for  $N = 20, 30, 40$ , respectively. The horizontal line in each panel corresponds to the fraction of reconstructed energy of the original dense POD-Galerkin projection model. In these panels, squares are used to denote data for  $M/N = 2$ , while circles denote data for  $M/N = 3$ . First, we observe that systems for  $\rho = 1$  ( $\xi = 1$ ) do not reconstruct the entire kinetic energy captured by the original POD basis. This behaviour is due to the fact that the presence of the stability constraint (2.23d)-(b), even in the configuration of no sparsification  $\xi = 1$ , produces a slight rotation of the new basis. When  $\xi$  is increased lower densities and lower reconstructed kinetic energy are obtained. However, the model dimension affects the slopes of the curves, *i.e.* the larger the model size, the more the model can be sparsified without affecting the ability of the new basis to reconstruct kinetic energy. This indicates that the sparsification technique becomes more effective as the model complexity increases. This appears to be a general trend since a similar behaviour was observed in Rubini *et al.* (2020a) using the LASSO-based *a-posteriori* sparsification. A second major remark is that when the ratio  $M/N$  is increased, lower densities can be achieved for the same reconstructed energy whilst remaining within the feasibility region. Alternatively, rotating the original POD basis into subspaces of much larger dimension  $M$  give an increased flexibility to generate models capturing more energy for the same density.

### 3.4. Analysis of the rotated modal basis

We now move to the analysis of the rotated spatial and temporal basis functions (2.13). A system with  $M/N = 3$ ,  $N = 30$ , obtained for  $\xi = 3$ , soon before the solution falls into the infeasible region in figure 3.3-(a), is analysed. Figure 5-(a) shows the magnitude of entries of the rotation matrix  $\mathbf{X}$ , found from the solution of (2.23d). Figure 5-(b) shows the modal energies  $\tilde{\lambda}_i$  of the new decomposition of equation (2.14). Figure 5-(c) shows

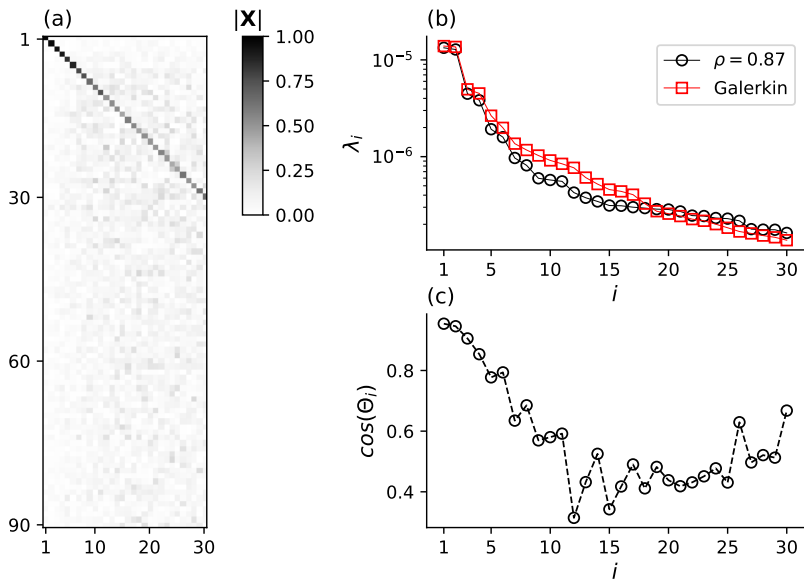


FIGURE 5. Optimisation results for the case  $M/N = 3$ ,  $N = 30$ ,  $\xi = 3$  (with density  $\rho = 0.87$ ). Panel (a): magnitude of the entries of the matrix  $\mathbf{X}$ . Panel (b): distribution of the modal energies of the original (square) and rotated (circles) basis functions. Panel (c): cosine of the angle between the modes of the original and rotated basis.

the cosine of the angle between the old and new sets of spatial modes, defined as

$$\cos(\theta_i) = \frac{(\phi_i, \tilde{\phi}_i)}{\|\phi_i\|_2 \|\tilde{\phi}_i\|_2}. \quad (3.1)$$

This quantity is clearly also the diagonal of  $\mathbf{X}$ , since  $\mathbf{X}^\top \mathbf{X} = \mathbf{I}$  holds. A general trend is observed. The high-energy modes are not significantly affected by the rotation while the opposite is true for the high-index, low-energy modes. More specifically, the first pair of eigenvalues, corresponding to the dominant fluid oscillation in the cavity, is virtually unchanged. This is then also observed for the first two spatial modes which are found to be almost collinear to the original ones, since  $\cos(\theta_{(1,2)}) \sim 0.9$ . A closer look at the rotation matrix  $\mathbf{X}$  shows that, for the first two columns, the elements on the diagonal are close to 1 while all other entries are close to zero. Conversely, a different trend emerges when low-energy modes are considered. Figure 5-(c) shows that the angle between the original and rotated modes increases with the modal index. We argue that this behaviour derives from the problem formulation (2.23d), constructed with the aim of generating a basis that minimises the energy loss with respect to the energetically optimal POD. As a result, the optimisation leaves unchanged the large and most energetic modes and rotates by a larger extent the less energetic modes to gain in sparsity. Figure 6 shows the out of plane vorticity component  $\omega$  for the original POD mode  $\phi_i$ , panels (a,d), and the rotated mode  $\tilde{\phi}_i$ , panels (b,e), for indices  $i = 1$  and  $19$ , respectively. The third column, panels (c,f), shows the absolute value of the difference between original and rotated modes. As expected, the first mode is not considerably affected by  $\mathbf{X}$ . On the other hand, mode  $i = 19$  is more pronouncedly affected by the rotation, with small scale features appearing all along the shear layer. We argue that the introduction of small scale

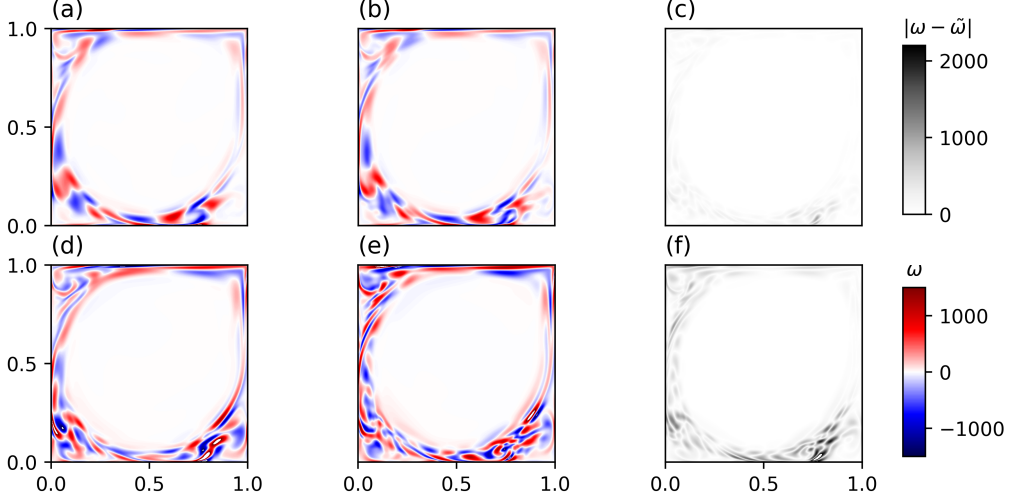


FIGURE 6. Vorticity field for the first mode POD mode, the first sPOD mode and the absolute value of their difference in panel (a),(b) and (c), respectively. Panels (d),(e) and (f) same quantities for  $i = 19$

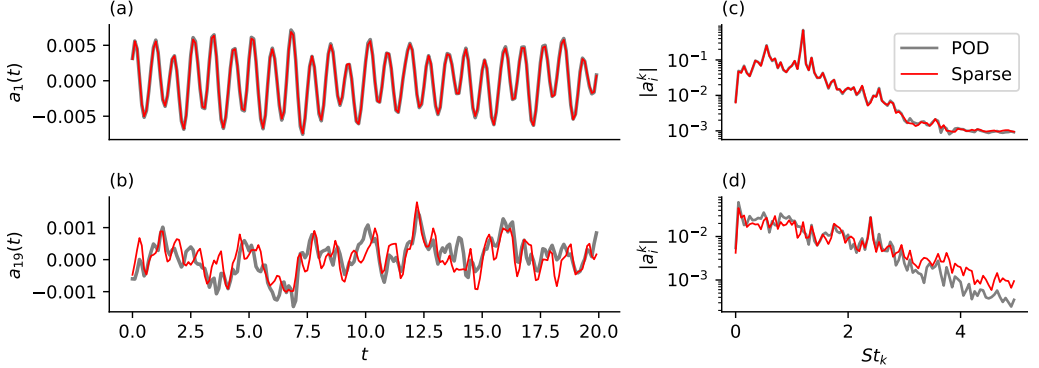


FIGURE 7. Temporal evolution and magnitude of the Fourier transform for  $a_1(t)$  in panels (a) and (c), respectively, and for  $a_{19}(t)$  in panels (b) and (d). Data is reported for the original POD temporal modes and for the rotated modes of the sparse system.

features is a combined effect of the stability constraint 2.23d, which enhances dissipation in the system (Balajewicz *et al.* 2016), and of the sparsity-promoting constraint (2.23d) since oscillatory modes are likely more effective in shrinking to zero the spatial averages involved in the projection coefficients (2.4). The temporal modes as defined in (2.13) are affected in a similar way. This is illustrated in figure 7 showing the temporal evolution of modes  $a_1(t)$  and  $a_{19}(t)$ , panels (a) and (b), and their amplitude spectra in panels (c) and (d), respectively. Since the first column of  $\mathbf{X}$  is close to zero, except for  $X_{11}$ , mode  $a_1(t)$  and its spectral content is not appreciably affected by the rotation, except for a small decrease of the amplitude due to decrease in energy content (see figure 5-(b)). Conversely, the spectral content of mode  $a_{19}(t)$  is remodulated by the rotation by introducing higher energy at high frequency components, consistent with the introduction of small scale features into the spatial mode.

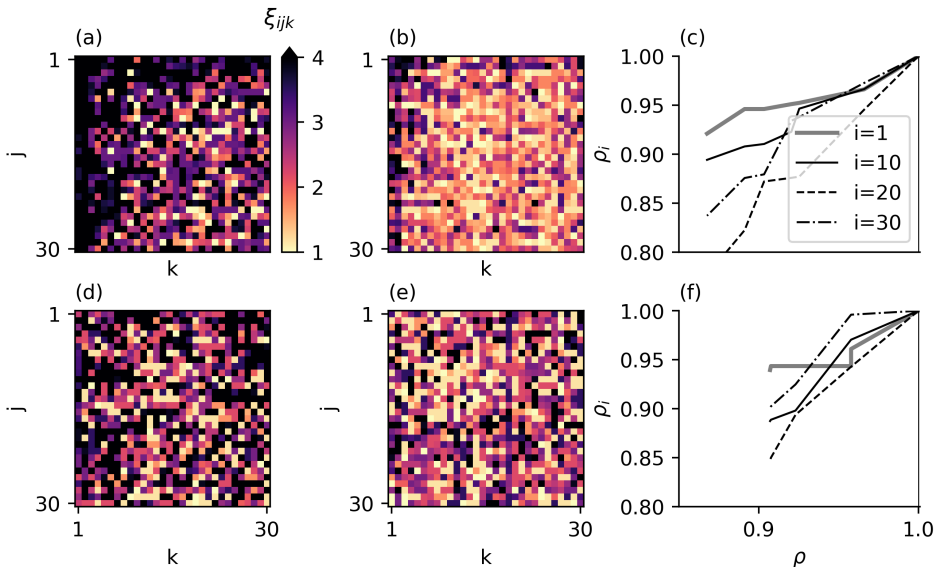


FIGURE 8. Distribution of the tensor  $\xi_{ijk}$  for  $i = 1, 30$  obtained solving the full problem P2 (2.23d) in panels (a) and (b), respectively. Panel (c): distribution of the curves  $\rho_i - \rho$  for the solution of the full model. Distribution of the tensor  $\xi_{ijk}$  for  $i = 1, 30$  obtained solving the incomplete problem P1 (2.23d) in panels (d) and (e), respectively. Panel (f): distribution of the curves  $\rho_i - \rho$  for the solution of the full model.

### 3.5. Subset of interactions identified in the sparse model

Even if the modification to the temporal and spatial modes is small in relative terms, it is sufficient to introduce sparsity in coefficient tensor  $\mathbf{Q}$  and the average triadic interaction tensor  $\mathbf{N}$  when the domain integrals (2.4) and the temporal averages (2.8) are computed.

To visualise how the sparsity varies when the penalisation weight  $\xi$  is increased, we introduce the tensor  $\boldsymbol{\xi}$  with entries  $\xi_{ijk}$  defined as the value of the penalisation parameter  $\xi$  in (2.23d) when the corresponding coefficient  $\tilde{Q}_{ijk}$  is first shrunk to zero. Figure 8 shows two slices of  $\boldsymbol{\xi}$  for  $i = 1$  and  $i = 30$ , for the model obtained at  $M/N = 3$  and  $N = 30$ . Panels (a) and (b) are obtained with the complete formulation P2 (including both the stability and sparsity promoting constraint), while panels (d) and (e), are obtained with the formulation P1 that only includes the sparsity promoting constraint. Panels (c) and (f) display the modal density  $\rho_i$ , defined as the density of the  $i$ -th ODE, as a function of the global density  $\rho$ , with  $\xi$  the curve parameter, for four modes across the hierarchy. For the complete formulation (P2), we observe that small-scale/small-scale interactions are the first interactions to disappear for moderate penalisation  $\xi$ . Increasing the penalisation, coefficients corresponding to interactions that are local in modal space are progressively pruned, leaving only coefficients capturing non-local interactions with the low-index modes for large penalisations. The structure of the sparse coefficient tensor obtained from the procedure is in agreement with the pattern of triadic energy interactions shown in figure 3.2-(b). Interestingly, figure 8(c) indicates that high-index modes can be sparsified more efficiently. This might be related to the fact that high-index modes are also more modified during the optimisation.

The key observation on the solution of the optimisation problem P1, bottom panels, is that the resulting sparsity pattern lacks the structure obtained with the complete formulation. In fact, even for small penalisations, coefficients corresponding to energy-



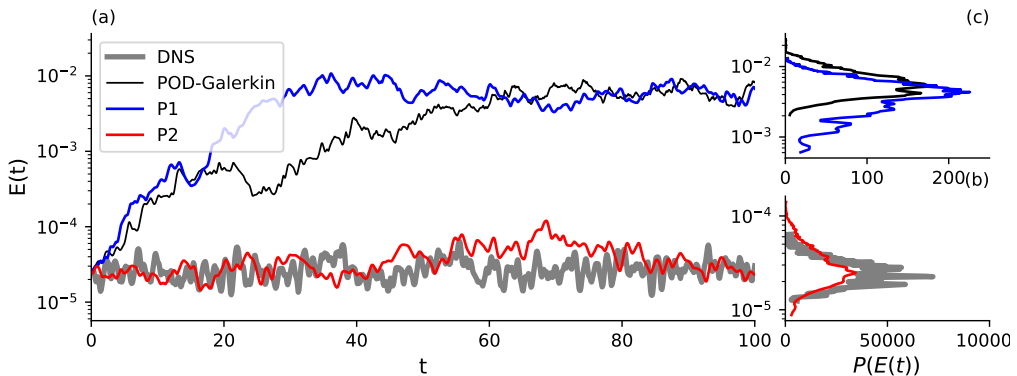


FIGURE 9. Temporal evolution of the turbulent kinetic energy  $E(t)$ . The performance of the two sparse models obtained by solving problem (2.23d) with and without the constraint (b) are compared against the DNS and the dense model obtained with Galerkin projection. Panels-(b,c) show the probability distribution of the level of  $E(t)$ .

relevant interactions are shrunk to zero. A random, chessboard-like coefficient distribution appears, even though similar global density are observed similar penalisation  $\xi$ . We argue that this is due to the fact that introducing a penalisation on the rotated tensor  $\tilde{\mathbf{Q}}$  without any constraint on the temporal evolution of the rotated system leads to a uniform reduction of the coefficients  $\tilde{Q}_{ijk}$  across all modes, because the strength of the energy interactions is not taken into account. Instead, since the coefficients  $Q_{ijk}$  are initially nonzero and do not have a clear structure (see figure 3.2-(a)), a uniform decrease of their magnitude across all modes will result in a chessboard-like structure. This behaviour can also be noticed in the shape of the  $\rho_i - \rho$  curves, panel (f), where modes are almost equally sparsified. This behaviour is consequence that, for the two formulations P1 and P2 of the problem, two different minima with similar value of the minimal density but with a different shape of the retained interactions have been found.

### 3.6. Temporal integration and energy analysis of the sparsified system

In this section, we analyse the properties of the sparse reduced order model under temporal integration and consider the triadic interactions tensor  $\mathbf{N}$  and the average energy budget (see equation (2.7)). The same configuration studied in previous sections, with  $M/N = 3$ ,  $N = 30$  and  $\xi = 3$ , is considered. Reduced order models obtained by solving problems P1 and P2 are considered. These models are integrated forward in time from an initial condition with an implicit time stepping scheme for a time-span equal to  $T = 500$  time units, from an initial condition obtained from one of the snapshots utilised for the POD. Figure 3.6-(a) shows the first one hundred time unity of the temporal evolution of the turbulent kinetic energy (2.5) for these two models, compared with the evolution from DNS and from the original POD-Galerkin model. Figure 3.6-(b,c) show the probability density function of the same quantity. As expected, the kinetic energy from the POD-Galerkin model simulation rapidly overshoots and converges towards energy levels about two orders of magnitude larger than the reference value from DNS. This behaviour is a well known result (see e.g. Noack *et al.* (2016); Östh *et al.* (2014)). Similarly, the sparse model obtained without any constraint on the temporal stability (problem P1) reproduce this behaviour. This can also be seen in the probability distribution functions in panels (b) and (c) of the turbulent kinetic energy showing that the two former models predict a larger value of the turbulent fluctuations. Conversely, the prediction of the sparsified and stabilised model (problem P2) matches

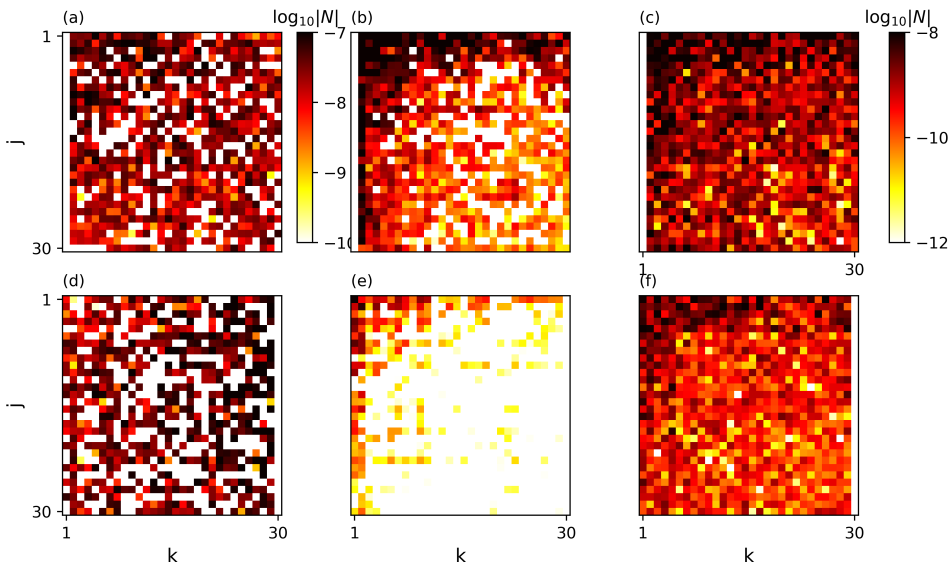


FIGURE 10. Value of  $N_{1jk}$  with the approaches P1 and P2 in panels (a,b). Value of  $N_{30jk}$  with P1 and P2 in panels (d,e). Value of  $N_{ijk}$  for a models only temporally stabilised for  $i = 1$  and  $i = 30$  in panels (c,f) respectively.

well the prediction of the DNS both as average value and amplitude of the fluctuations. This result clearly indicates the need of a tie back to the temporal evolution of the system in order to obtain meaningful results.

Once obtained the new sets of temporal modes, the triadic interactions tensor  $\mathbf{N}$  and linear term  $\tilde{L}_{ii}\tilde{a}_i\tilde{a}_i$  can be computed. Figure 3.6 show two slices for  $i = 1, 30$  (first and second row, respectively) of the average triadic interaction tensor  $\mathbf{N}$  for the three different models previously considered. Namely, P1 approach with only the sparsity promoting constraint active in panels (a) and (d), P2 approach with all the constraints active in panels (b) and (e). In the third column, panels (c) and (f) the same quantity for a system obtained only with the temporal stability constraint is shown. The differences between the complete formulation P2 and the partial one P1 are mainly two. First, the two problems identify a different pattern of interactions where only the complete formulation P2 is coherent with the shape of the energetic interactions 3.2-(b). This is direct consequence of the shape of  $\mathbf{Q}$  already discussed in the previous section. Second, the relative strength of the identified interactions across the hierarchy of structure in the plane  $j - k$  is not physically consistent for the case with the partial formulation P1. This is a consequence of the lack of dissipation and the consequent over-prediction on the amplitude fluctuations of the  $\tilde{a}_i$  with high index  $i$ . For completeness in panels (c) and (f) we display the result obtained in the case where only the constraint 2.28-(b) is present. Interestingly, we observe that, although no sparsity is promoted, the presence of the temporal stability constraint is sufficient to re-scale the temporal fluctuation to the correct value. This result shows the importance of the conjoint effect of the temporal stability and sparsity promoting constraint to produce an effective sparsification in agreement with the physics of the triadic interactions.

To visualise the overall structure of the tensor  $\mathbf{N}$  across the hierarchy of modes  $i = 1, \dots, N$  we apply the methodology explained in the energy analysis section. To characterise which regions of  $\mathbf{N}$  are more active in the average energy transfer, the sum of the absolute values of the entries  $N_{ijk}$  for the four different areas  $LL, SS$  and  $LS$

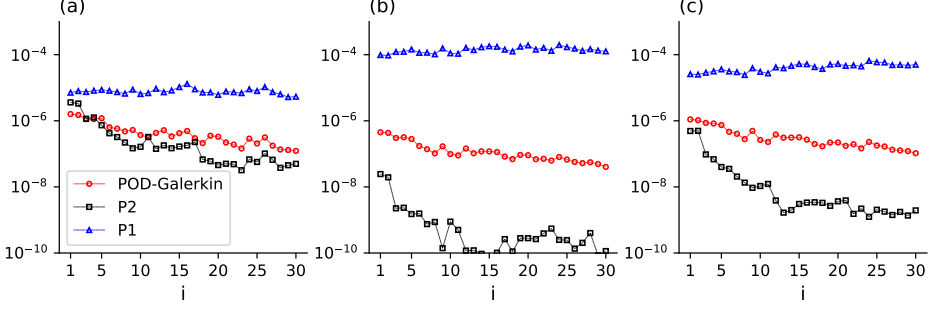


FIGURE 11. Value of the sum of the absolute value of  $N_{ijk}$  for the different models in the three regions of  $\mathbf{N}$  defined in figure 3.2-(b). Panel (a),(b) and (c) show the regions  $LL$ ,  $SS$  and  $LS$ , respectively.

as defined in figure 3.2-(b) is computed. Figure 3.6 shows the value of  $LL$ ,  $SS$  and  $LS$  in panel (a),(b) and (c), respectively. Different trends for the two models P1 and P2 with respect to the model obtained by POD-Galerkin are observed. First, we consider panel (a) containing the  $LL$  interactions. We observe that the value provided by the P2 formulation is very similar to the projection model obtained by DNS with the only difference of a slightly lower value due to the presence of the constraint on  $\mathbf{Q}$ . In addition, the model obtained with the P2 approach has the same decay as the projection model (DNS). Conversely, the P1 model does not present any decay of the energy level across the hierarchy of modes. This trend of the model obtained with the P1 approach is shown also in the interactions of the region  $SS$  and  $LS$ , in panels (b) and (c), respectively. This is consequence of the over prediction in the amplitude of the temporal fluctuations especially observed for the modes with high modal index  $i$ . In addition, in panel (b) and (c) we observe than on average the value of the model P2 is lower than the one obtained by projection, this effect is much weaker with respect to the interaction of the region  $LL$ . This confirms a consistent sparsification where the less relevant interactions, mainly present in the regions  $SS$  and  $SL/LS$ , are more heavily pruned than interactions present in the region  $LL$ . More interestingly, we observe that the numerical difference between P2 and the DNS in panel (b) and (c) grows as we move towards larger values of  $i$  showing that high-index modes are more effectively sparsified as already shown in figure 8-(c). To conclude we observe that none of these effects are present for the P1 model confirming this approach not suitable for a physically consistent sparsification.

We now analyse the mode by mode the linear and quadratic energy transfer terms as defined in the mean average energy balance (2.7). In figure 12 we consider three different systems: the one obtained by Galerkin projection onto the POD subspace in panels (a) and (d), the one obtained solving the problem P2 in panels (b) and (e) and solving problem P1 in panels (c) and (f). The model obtained by projection is analysed first. In panel (a) the linear term in (2.7) obtained by POD-Galerkin projection is shown. We observe a large production of kinetic energy in the first modes and a moderate dissipation in the last ones. Overall this results into an unbalance between production and dissipation leading to the over prediction of kinetic energy shown in figure 3.6-(a). The non linear term  $T_i$  shown in panel (d), instead, displays the correct energy cascade from the large (negative values of for small  $i$ ) to the small scales (positive values for  $i$  large) already observed for two dimensional turbulent flows. Second, we consider a model obtained by the solution of the complete optimisation problem (P2) in panels (b) and (e). Panel (b) shows that for this case the production/dissipation is better balanced with

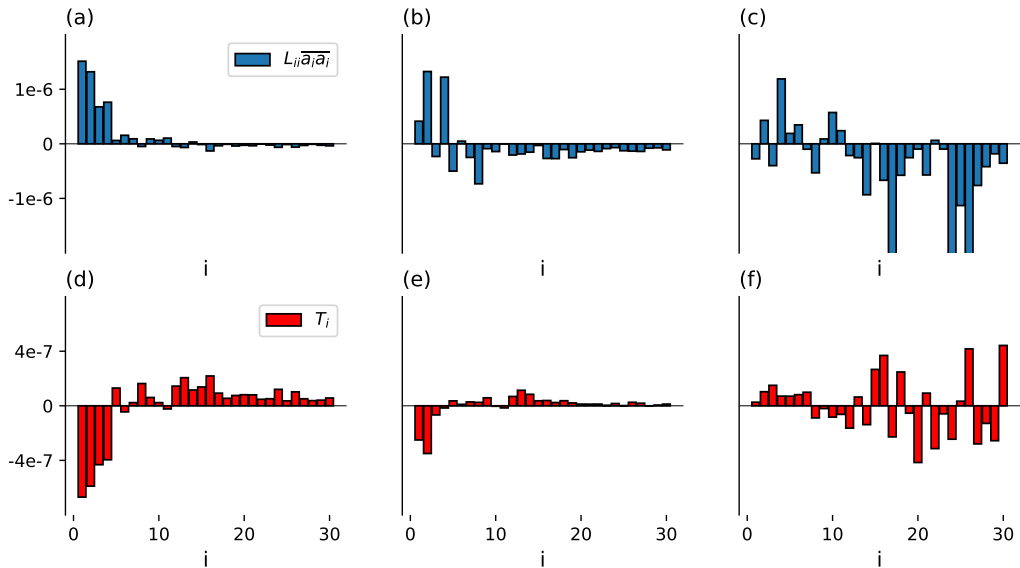


FIGURE 12. Value of the linear term  $L_{ii}a_i a_i$  in (2.7) for the Galerkin projection, the P2 and the P1 approach in panel (a),(b) and (c), respectively. Value of the quadratic term  $T_i$  in (2.7) for the Galerkin projection, the P2 and the P1 approach in panel (d),(e) and (f), respectively.

lower production in the low index modal structure and larger dissipation in the high index modes. In addition, the P2 approach also manages to preserve the right shape of the nonlinear energy transfer between modes as displayed in panel (e).

Conversely, the absence of the constraint in the optimisation problem (formulation P1) does not provide any balance of the turbulent kinetic energy budget (2.7). Both the linear and the quadratic term are off with respect the value and the shape obtained in for the POD-Galerkin model shown in panels (a) and (d). In addition, the nonlinear energy transfer appears to be uniformly diminished and reshuffled losing physicality of the corresponding modal decomposition as shown in panel (f). The largest values of  $T_i$  for the high index modes is consequence of the unphysically large value of the fluctuations in the high index temporal coefficients.

These results show that to obtain a sparse model that is consistent with the physics of the flow it is of paramount importance to introduce in the sparsification algorithm some information about the dynamics or the physics of the flow. This is consistent with what observed by Loiseau & Brunton (2018) that proved the need of additional constraint on the energy conservation to enhance the temporal accuracy of dynamical system reconstructed from data. Similarly, Rubini *et al.* (2020a) observed that including the temporal dynamics  $\dot{a}_i$  in the sparsification preserve the correct energy transfer in sparsified dynamical system of turbulent flows.

## 4. Conclusions

In this paper we presented an *a priori* sparsification methodology for Galerkin-based reduced order models of turbulent flows. The approach aims to generate a set of modal structures that result in a Galerkin model with the quadratic coefficient tensor  $\mathbf{Q}$  regulating triadic interaction possessing a sparse structure. As opposed to our previous  $l_1$ -regression based sparsification approach (Rubini *et al.* 2020a), where interactions are tuned *a-posteriori* given a set of basis functions, the objective of the present methodology is to maintain a closer correspondence between the modal structures and the Galerkin model.

The work is motivated by established knowledge on scale interactions in turbulence, where dynamics at a certain length scale depends most prominently on a subset of other scales. State-of-the-art modal decomposition techniques are either data-driven or result from the analysis of an operator. These do not necessarily leverage the physics of scale interactions and therefore the opportunities for computational saving and increased interpretability offered by sparsity. In addition, as observed in our previous work (Rubini *et al.* 2020a), the sparsity of inter-modal energy transfers is not invariant under a change of the subspace utilised for projection. This, in turn, implies that the nature of interactions between coherent structures can greatly depend on the mathematical representation of the flow kinematics. This suggests that it might be of interest to find one representation from which the organisation of interactions is particularly insightful or revealing. In addition to the recent work of (Schmidt 2020), this paper is one attempt at addressing this question.

Computationally, our methodology rests on space-only Proper Orthogonal Decomposition (POD) as a starting point, since energy interactions between triads of POD modes display a wide range of intensity, with a large fraction of transfers not contributing significantly to the dynamics. Hence, the idea is to seek a small rotation of the original POD subspace (of dimension  $N$ ) within a larger POD subspace (of dimension  $M > N$ ) so that model coefficients and thus energy interactions have a sparse structure. In practice, this is achieved by solving a non-convex optimisation problem, where we seek a rotation matrix  $\mathbf{X}$  that minimises energy losses with respect to the original POD basis. An inequality constraint involving the  $l_1$  norm of the rotated quadratic coefficient tensor is included to promote sparsity. This formulation is augmented with a further constraint that enforces long-term temporal stability of the Galerkin model. For this purpose, the *a-priori* stabilisation approach proposed by Balajewicz *et al.* (2016) is employed as it fits naturally within the proposed subspace-rotation-based formulation. Considering the sparsity of quadratic interactions as a key driver in our methodology comes at the cost of losing guarantees on the uniqueness of the solution. In fact, unlike state-of-the-art decomposition methods, whereby strong uniqueness and convexity properties apply, here different initial guesses in the optimisation can lead to different sets of modes. However, we provide evidence that the optimisation process is repeatable if a small perturbation of the identity matrix, as initially desired, is chosen as initial guess in the optimisation.

As a demonstration, we considered two-dimensional lid-driven cavity flow at Reynolds number  $Re = 2 \times 10^4$ , where the motion is chaotic and energy interactions are scattered in modal space. Sparse models generated by varying the regularisation weight  $\xi$  in the sparsity promoting constraint have been visualised onto the reconstructed energy - model density plane. Results show that the energy reconstruction - sparsity trade off depends on the model size  $N$  and the ratio  $M/N$ . In particular, larger models can be more sparsified with less impact on the energy reconstruction ability. On the other hand, lower densities can be obtained by rotating the original POD basis within larger sub-spaces (a

higher ratio  $M/N$ ), since the increased flexibility allows satisfying the sparsity promoting constraint even for relatively larger regularisation weights  $\xi$ . Hence, a minimal density can be defined. This is a clear advantage with respect to regression based methods, where the regularisation weight is a free parameter that needs to be carefully chosen by the user.

A deeper analysis shows that the structure of the inter-modal energy interactions in the rotated model is qualitatively similar to that of the original POD-Galerkin system. More specifically, coefficients of the quadratic interaction tensor corresponding to large-scale/large-scale and the large-scale/small-scale interactions are preserved, but those defining the weak small-scale/small-scale interactions are pruned during the optimisation. This result is in agreement with the established picture of triadic interactions in two dimensional flows and with previous results of sparsification of reduced order models of two dimensional flows (Rubini *et al.* 2020a,b). More interestingly, we observed that a physically-consistent distribution of interactions and a stable long-term behaviour can only be obtained by augmenting the sparsification procedure with a temporal stability constraint. In fact, it was observed that models obtained without such constraint can inherit well-known temporal stability issues of dense POD-Galerkin model.

Some challenges and avenues for future work are now discussed. First, the present *a-priori* sparsification technique produces relatively less sparse Galerkin models than the *a posteriori* LASSO-based approach considered in Rubini *et al.* (2020a). We argue that this is likely the consequence of accepting a stronger consistency between the modal structures and the Galerkin model.

In section 2 we observed the complex structure of the sparsity promoting constraint  $\|\tilde{\mathbf{Q}}\|_1$  in the  $\mathbf{X}_{ij}$  space. More specifically, is remarkable the presence of several minima and valley of minima with similar values of  $\|\tilde{\mathbf{Q}}\|_1$ . This is mathematically consequence of the non-convexity of the optimisation problem and poses the question about the physical interpretations of so many different solution of the same optimisation problem. We speculate that this s consequence of the attempt of describing through globally defined basis functions  $\phi_i$  flow structure (vortexes) that interacts locally in physical space. We argue that this feature in the physical space can be somehow ported into the modal space. However, what we are trying to achieve with our methodology is somehow try to "change the point of view" such that the number of interacting modal structures is minimal in the  $l_1$  sense. It is in the author opinion that a modal representation based of the interactions could not be the best way to represent the flow in term of the locality of the interactions in the spatial space. An interesting avenue to explore in the future could be to develop a modal decomposition where the modes have a compact local support could be the key enabler to obtain a representation in term of the sparsity.

A second challenge is that, by construction, the optimisation is performed on all modal structures simultaneously, which can become a large, computationally expensive task. A potential avenue to mitigate these costs could be to construct the basis structures in a recursive fashion.

The authors gratefully acknowledge support for this work from the Air Force Office of Scientific Research (Grant No. FA9550-17-1-0324, Program Manager Dr D. Smith).

## Appendix A. Computation of the Gradients

### A.1. Gradient of the Objective function

$$\frac{\partial Obj}{\partial \mathbf{X}} = -(\mathbf{A}^\top + \mathbf{A})\mathbf{X} = -2\mathbf{A}^\top \mathbf{X} \quad (\text{A } 1)$$

### A.2. Gradient of the stability constraint

$$Tr(\mathbf{X}^\top \mathbf{L} \mathbf{X}) \quad (\text{A } 2)$$

$$\frac{\partial}{\partial \mathbf{X}} Tr(\mathbf{X}^\top \mathbf{L} \mathbf{X}) = \frac{\partial}{\partial \mathbf{X}} (\mathbf{X}^\top \mathbf{L} \mathbf{X}) = (\mathbf{L}^\top + \mathbf{L})\mathbf{X} \quad (\text{A } 3)$$

### A.3. $l_1$ part of the objective function

$$\|\tilde{\mathbf{Q}}\|_1 \quad (\text{A } 4)$$

The tensor  $\tilde{\mathbf{Q}}$  is computed as a rotation of the tensor  $\mathbf{Q}$  as in 2.15. Its derivative with respect to the transformation matrix  $\mathbf{X}$

$$\frac{\partial \|\tilde{Q}_{ijk}\|_1}{\partial X_{mn}} = \frac{\partial \tilde{Q}_{ijk}}{\partial X_{mn}} \frac{\tilde{Q}_{ijk}}{|\tilde{Q}_{ijk}|} \quad (\text{A } 5)$$

to compute the derivative of  $\tilde{Q}_{ijk}$  we proceed computing how this quantity changes as we add a small variation to the value of  $\mathbf{X} + d\mathbf{X} = \mathbf{X} + \epsilon \mathbf{X}$

$$\frac{\partial \tilde{\mathbf{Q}}}{\partial \mathbf{X}} = \lim_{\epsilon \rightarrow 0} \frac{\tilde{\mathbf{Q}}(\mathbf{X} + \epsilon \mathbf{X}) - \tilde{\mathbf{Q}}(\mathbf{X})}{\epsilon} \quad (\text{A } 6)$$

expanding this expression in Einstein notation and retaining only the zero order terms in  $\epsilon$  we obtain

$$d\tilde{Q}_{ijk} = Q_{pqr}(X_{pi}X_{qj}dX_{kr} + X_{pi}X_{rk}dX_{jq} + X_{rk}X_{qj}dX_{pi}) \quad (\text{A } 7)$$

using the identity  $dX_{kr} = dX_{mn}\delta_{km}\delta_{rm}$  to rewrite the variation with respect to the indexes  $m, n$ .

$$d\tilde{Q}_{ijk} = \frac{\partial \tilde{Q}_{ijk}}{\partial X_{mn}} dX_{mn} = Q_{pqr}(X_{pi}X_{qj}\delta_{km}\delta_{rm} + X_{pi}X_{rk}\delta_{jn}\delta_{qm} + X_{rk}X_{qj}\delta_{in}\delta_{pm})dX_{mn} \quad (\text{A } 8)$$

we finally obtain

$$\frac{\partial \tilde{Q}_{ijk}}{\partial X_{mn}} = Q_{pqr}(X_{pi}X_{qj}\delta_{kn}\delta_{rm} + X_{pi}X_{rk}\delta_{jn}\delta_{qm} + X_{rk}X_{qj}\delta_{in}\delta_{pm}) \quad (\text{A } 9)$$

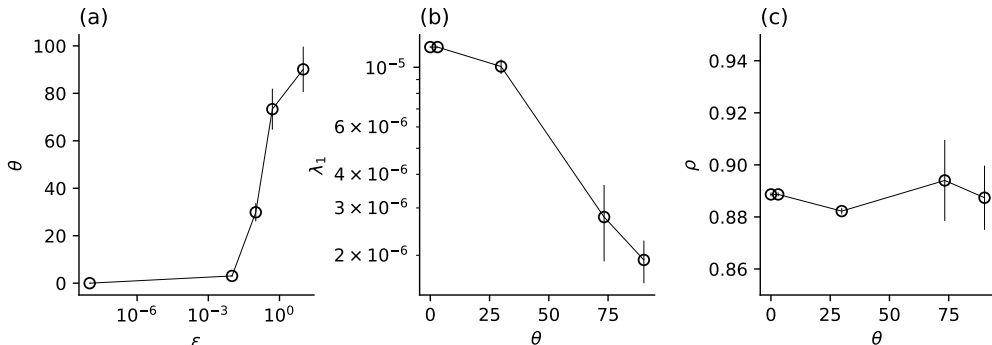


FIGURE 13. Panel (a): relation between the value of the perturbation  $\epsilon$  and the average rotation angle between sub-spaces  $\theta$ . Mean values and standard deviation for the first eigenvalue  $\lambda_1$  and density  $\rho$  for the different system obtained, in panel (b) and (c) respectively.

## Appendix B. Dependence of the solution from the initial condition

### B.1. About the uniqueness of the solution

Problem (2.23d) is non-convex due to the constraint on the quadratic interactions tensor  $\mathbf{Q}$ . This introduces the problem of characterising the uniqueness and the quality of the solution with respect to other local minima. To understand how this problem affects the optimisation results, we considered different sets of initial guesses defined as increasingly larger perturbations of the identity, *i.e.*:

$$\mathbf{X}_0 = \begin{bmatrix} \mathbf{I} \\ \mathbf{0} \end{bmatrix} + \epsilon \mathbf{R}, \quad (\text{B } 1)$$

with  $\mathbf{R} \in \mathbb{R}^{M \times N}$  a randomly generated rotation matrix, satisfying  $\mathbf{R}^\top \mathbf{R} = \mathbf{I}$ , with  $\mathbf{I} \in \mathbb{R}^{N \times N}$ . We generated ten random rotation matrices for  $\epsilon$  in the range  $[10^{-8}, 10]$  and solved problem (2.23d) keeping  $\xi = 2$  to target an intermediate density and ensure to fall into the feasibility region. Figure B.1-(a) shows the effects of  $\epsilon$  on the average rotation angle  $\theta$  between columns of the initial guess matrix  $\mathbf{X}_0$  and column of the matrix  $[\mathbf{I}, \mathbf{X}_0]^\top$ . Circles and vertical bars identify the average and standard deviation of this quantity across the ten different samples. In panel (b) and (c), we show these statistics for the eigenvalue  $\lambda_1$  [NOTA for  $e_n$ ] and the density  $\rho$ , respectively, as a function of the  $\theta$ . Results show that for low  $\theta$ , all the initial guesses converge to the same solution. Conversely, when initial guesses starting from regions farther away from the identity the standard deviations between the different solutions starts growing, as problem 2.23d converges to different solutions. This result is expected and it is in agreement with the shape of the sparsity constraint shown in figure 2.3-(a). This supports the initial hypothesis of looking for solutions as small rotations of the POD basis. In addition, we observe that  $\lambda_1$  decreases monotonically with the size of the perturbation, since the farther is the initial guess from the identity, the larger is the loss of energetic optimality. A different behaviour is observed for the density where the average value is comparable for all initial guesses considered.

## Appendix C. Computational cost

The sparsity promoting constraint involves polynomial functions of the optimisation variables and analytical expressions of the gradients can be obtained, scaling down com-



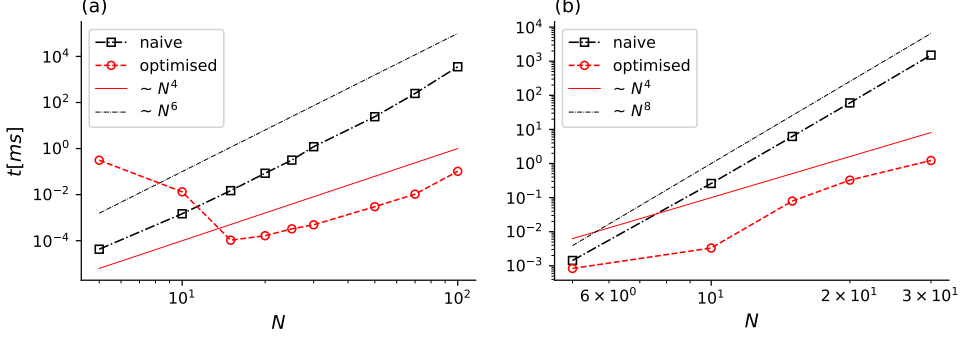


FIGURE 14. Computational cost in milliseconds required for one evaluation of  $\tilde{\mathbf{Q}}$  and  $\frac{\partial ||\tilde{\mathbf{Q}}||_1}{\partial \mathbf{X}}$  in panel (a) and (b), respectively. For this example  $M = N$  was chosen.

putational costs by several orders of magnitude. The gradient of the sparsity promoting constraint with respect to the rotation matrix  $\mathbf{X}$  is

$$\frac{\partial ||\tilde{\mathbf{Q}}_{ijk}||_1}{\partial X_{mn}} = \frac{\partial \tilde{\mathbf{Q}}_{ijk}}{\partial X_{mn}} \frac{\tilde{\mathbf{Q}}_{ijk}}{|\tilde{\mathbf{Q}}_{ijk}|} \quad (\text{C } 1)$$

where the Einstein notation is used and can be expanded with Kronecker's delta  $\delta_{ij}$  (see appendix A.1) as

$$\frac{\partial \tilde{\mathbf{Q}}_{ijk}}{\partial X_{mn}} = \mathbf{Q}_{pqr} (X_{pi} X_{qj} \delta_{kn} \delta_{rm} + X_{pi} X_{rk} \delta_{jn} \delta_{qm} + X_{rk} X_{qj} \delta_{in} \delta_{pm}). \quad (\text{C } 2)$$

However, a naive implementation of this expression leads to the scaling  $\mathcal{O}(N^4 M^4)$ , since the tensor expression involves 8 indices. Evaluating the constraint ((2.23d)), instead, involves six tensor indices, with computational costs scaling as  $\mathcal{O}(N^3 M^3)$ . The scaling of costs is shown in figure C, which, for simplicity assume  $N = M$ . However, a more detailed analysis of the tensor operations involved in the evaluation the constraint and its gradient (see Pfeifer *et al.* (2014)) shows that some of operations involving summations over  $M$  are repeated and can be thus factored out. This key observation enables reducing computational cost to  $\mathcal{O}(MN^3)$  for both the constraint and its gradient, as shown in figure C.

## REFERENCES

- ARBABI, H. & MEZIĆ, I. 2017 Study of dynamics in post-transient flows using Koopman mode decomposition. *Physical Review Fluids* **2** (12), 124402.
- AUTERI, F., PAROLINI, N. & QUARTELLA, L. 2002 Numerical investigation on the stability of singular driven cavity flow. *Journal of Computational Physics* **183** (1), 1–25.
- BALAJEWICZ, M., DOWELL, E. & NOACK, B. 2013 Low-dimensional modelling of high-Reynolds-number shear flows incorporating constraints from the Navier–Stokes equation. *Journal of Fluid Mechanics* **729**.
- BALAJEWICZ, MACIEJ, TEZAU, IRINA & DOWELL, EARL 2016 Minimal subspace rotation on the stiefel manifold for stabilization and enhancement of projection-based reduced order models for the compressible navier–stokes equations. *Journal of Computational Physics* **321**, 224–241.
- BRASSEUR, J. & WEI, C. 1994 Interscale dynamics and local isotropy in high reynolds number turbulence within triadic interactions. *Physics of Fluids* **6**.
- BRUNTON, S. L., PROCTOR, J. L. & KUTZ, J. N. 2016 Discovering governing equations from data by sparse identification of nonlinear dynamical systems. *Proceedings of the National Academy of Sciences* **113** (15).
- CAZEMIER, W., VERSTAPPEN, R. W. C. P. & VELDMAN, A. E. P. 1998 Proper orthogonal decomposition and low-dimensional models for driven cavity flows. *Physics of fluids* **10** (7), 1685–1699.
- COUPLET, M., SAGAUT, P. & BASDEVANT, C. 2003 Intermodal energy transfers in a proper orthogonal decomposition–galerkin representation of a turbulent separated flow. *Journal of Fluid Mechanics* **491**.
- CRAIK, ALEX DD 1971 Non-linear resonant instability in boundary layers. *Journal of Fluid Mechanics* **50** (2), 393–413.
- DOMARADZKI, J ANDRZEJ, LIU, WEI, HÄRTEL, CARLOS & KLEISER, LEONHARD 1994 Energy transfer in numerically simulated wall-bounded turbulent flows. *Physics of Fluids* **6** (4), 1583–1599.
- FICK, L., MADAY, Y., PATERA, A. T. & TADDEI, T. 2018 A stabilized POD model for turbulent flows over a range of reynolds numbers: Optimal parameter sampling and constrained projection. *Journal of Computational Physics* **371**, 214 – 243.
- FRIEDMAN, J., HASTIE, T. & TIBSHIRANI, R. J. 2008 *The Elements of Statistical Learning*. Springer.
- GALLETTI, B, BRUNEAU, CH, ZANNETTI, LUCA & IOLLO, ANGELO 2004 Low-order modelling of laminar flow regimes past a confined square cylinder. *Journal of Fluid Mechanics* **503**, 161–170.
- JIN, BO, SYMON, SEAN & ILLINGWORTH, SIMON J 2020 Energy transfer mechanisms and resolvent analysis in the cylinder wake. *arXiv preprint arXiv:2004.14534* .
- JOHNSON, STEVEN G 2014 The nlopt nonlinear-optimization package.
- KOLMOGOROV, ANDREI NIKOLAEVICH 1991 The local structure of turbulence in incompressible viscous fluid for very large reynolds numbers. *Proceedings of the Royal Society of London. Series A: Mathematical and Physical Sciences* **434** (1890), 9–13.
- KRAICHNAN, R. H. 1971 Inertial-range transfer in two-and three-dimensional turbulence. *Journal of Fluid Mechanics* **47** (3), 525–535.
- LAVAL, J. P., DUBRULLE, B. & NAZARENKO, S. 1999 Nonlocality of interaction of scales in the dynamics of 2D incompressible fluids. *Physical Review Letters* **83** (20), 4061.
- LOISEAU, J. C. & BRUNTON, S. L. 2018 Constrained sparse Galerkin regression. *Journal of Fluid Mechanics* **838**, 42–67.
- LUMLEY, J. L. 1970 Stochastic tools in turbulence. *Tech. Rep.*
- MOFFATT, HK 2014 Note on the triad interactions of homogeneous turbulence. *Journal of Fluid Mechanics* **741**.
- NOACK, B., MORZYNSKI, M. & TADMOR, G. 2011 *Reduced-order modelling for flow control*, , vol. 528. Springer Science & Business Media.
- NOACK, B. R. & ECKELMANN, H. 1994 A Global Stability Analysis of the Steady and Periodic Cylinder Wake. *Journal of Fluid Mechanics* **270**, 297–330.
- NOACK, BERND R, PAPAS, PAUL & MONKEWITZ, PETER A 2005 The need for a pressure-term

- representation in empirical galerkin models of incompressible shear flows. *Journal of Fluid Mechanics* **523**, 339–365.
- NOACK, B. R., STANKIEWICZ, W., MORZYŃSKI, M. & SCHMID, P. J. 2016 Recursive dynamic mode decomposition of transient and post-transient wake flows. *Journal of Fluid Mechanics* **809**, 843–872.
- OHKITANI, K. 1990 Nonlocality in a forced two-dimensional turbulence. *Physics of Fluids A: Fluid Dynamics* **2** (9), 1529–1531.
- ÖSTH, J., NOACK, B. R., KRAJNOVIĆ, S., BARROS, D. & BORÉE, J. 2014 On the need for a nonlinear subscale turbulence term in pod models as exemplified for a high-reynolds-number flow over an ahmed body. *Journal of Fluid Mechanics* **747**, 518–544.
- PENG, Y. H., SHIAU, Y. H. & HWANG, R. R. 2003 Transition in a 2-D lid-driven cavity flow. *Computers & Fluids* **32** (3), 337 – 352.
- PFEIFER, ROBERT N. C., HAEGEMAN, JUTHO & VERSTRAETE, FRANK 2014 Faster identification of optimal contraction sequences for tensor networks. *Phys. Rev. E* **90**, 033315.
- POPE, S. B. 2001 Turbulent flows.
- REMPFER, D. & FASEL, H. F. 1994a Dynamics of three-dimensional coherent structures in a flat-plate boundary layer. *Journal of Fluid Mechanics* **275**, 257–283.
- REMPFER, D. & FASEL, H. F. 1994b Evolution of three-dimensional coherent structures in a flat-plate boundary layer. *Journal of Fluid Mechanics* **260**, 351–375.
- ROWLEY, C. W. & DAWSON, S. T. M. 2017 Model reduction for flow analysis and control. *Annual Review of Fluid Mechanics* **49**, 387–417.
- RUBINI, RICCARDO, LASAGNA, DAVIDE & DA RONCH, ANDREA 2020a  $l_1$ -based sparsification of energy interactions in two-dimensional turbulent flows. *arXiv preprint arXiv:2006.05736*.
- RUBINI, RICCARDO, LASAGNA, DAVIDE & DA RONCH, ANDREA 2020b  $l_1$ -based calibration of pod-galerkin models of two-dimensional unsteady flows. *Chinese Journal of Aeronautics*.
- SCHLEGEL, M. & NOACK, B. R. 2015 On long-term boundedness of galerkin models. *Journal of Fluid Mechanics* **765**, 325–352.
- SCHMID, P. J. 2010 Dynamic mode decomposition of numerical and experimental data. *Journal of Fluid Mechanics* **656**, 5–28.
- SCHMIDT, OLIVER T 2020 Bispectral mode decomposition of nonlinear flows. *arXiv preprint arXiv:2002.04146*.
- SVANBERG, KRISTER 2014 A class of globally convergent optimization methods based on conservative convex separable approximations. *SIAM Journal on Optimization* pp. 555–573.
- SYMON, SEAN, ILLINGWORTH, SIMON J & MARUSIC, IVAN 2020 Energy transfer in turbulent channel flows and implications for resolvent modelling. *arXiv preprint arXiv:2004.13266*.
- TAIRA, K., BRUNTON, S. L., DAWSON, S. T. M., ROWLEY, C. W., COLONIUS, T., MCKEON, B. J., SCHMIDT, O. T., GORDEYEV, S., THEOFILIS, V. & UKEILEY, L. S 2017 Modal analysis of fluid flows: An overview. *AIAA Journal* pp. 4013–4041.
- TERRAGNI, F., VALERO, E. & VEGA, J. M. 2011 Local POD plus galerkin projection in the unsteady lid-driven cavity problem. *SIAM Journal on Scientific Computing* **33** (6), 3538–3561.
- TIBSHIRANI, R. J. 2013 The LASSO problem and uniqueness. *Electronic Journal of Statistics* **7**, 1456–1490.
- TOWNE, A., SCHMIDT, O. T. & COLONIUS, T. 2018 Spectral proper orthogonal decomposition and its relationship to dynamic mode decomposition and resolvent analysis. *Journal of Fluid Mechanics* **847**, 821–867.